

Analytical Pumping Speed Models for Electric Propulsion Vacuum Facilities

R. Spektor, T. S. Matlock, M. W. Crofton, and D. T. Schoeffler
The Aerospace Corporation

L. Brieda
Particle in Cell Consulting, LLC

Two analytical models for computing the pumping speed of a vacuum chamber were derived. The models focus on the vacuum systems used for testing electric propulsion devices. The Node model is based on a well-known calculation of the effective pumping speed adjusted by the conductance between the pump and the measurement location. The Flux model is derived by balancing particle fluxes at two temperatures – one at the ambient condition, such as the chamber walls, and second at a cold temperature indicative of the cryo-pumps. The model also takes into account gas-wall interaction. The Flux model produces the flux transfer matrices that reduce the pumping speed calculation to a linear algebraic problem. Both models produced a good agreement with the experimentally measured pumping speed for two chambers investigated in this paper. The Flux model prediction of the pumping speed for a new chamber that is currently under design was twice as high as the pumping speed predicted by the Node model and within 30% of a PIC simulation that used the CTSP code.

I. INTRODUCTION

Inability to achieve adequately low pressure in the available vacuum chambers presents a significant challenge to testing the new generation of high power Electric Propulsion (EP) devices.¹ Recent findings showing that a long-held guidance of 10^{-5} Torr as the minimum pressure necessary to test a Hall thruster is inadequate to expose important performance, stability, plume divergence, and EMI issues that may not be present during the ground tests but exhibit themselves in the low vacuum of space.²⁻⁵ These findings highlight the need to develop more capable ground test facilities, which can achieve pressure levels significantly below the 10^{-5} Torr recommendation.

Designing an EP testing facility is an iterative, slow, and costly process. Multiple pumping surfaces are usually employed in the modern vacuum facilities. Extensive numerical simulations are required to optimize locations of these pumps in order to achieve the lowest possible chamber pressure. These simulations can often be time-consuming and expensive. While not completely obviating the need for these simulations, we propose in this paper two straightforward analytical models for calculating the effective pumping speed of a chamber. The models allow quick and simple initial design iterations before the final validation with a sophisticated numerical simulation. Such simple tools may help in reducing initial design iteration times, enabling faster convergence to the best solution, greater design flexibility, and therefore reducing the overall project cost. While the emphasis is placed on the cryogenically pumped systems with a thruster operating on xenon gas, both models can be applied to any type of pumps and any type of gas.

Most modern vacuum chambers used for EP testing utilize cryogenic pumps operated at temperatures around 20 K in order to achieve significant pumping speed. Temperatures up to approximately 50 K can be used for pumping xenon, but the pumping speed and the ultimate pressure scale inversely with the cryogenic surface temperature. On the other hand, operating at a temperature above 20 K typically allows greater heat

rejection capacity. Thus a tradeoff between the cryopumping surface temperature and the heat rejection capacity needs to be carefully considered in the design of such a system. A figure of merit often used for cryogenic pumps operating at 20 K is $55,000 \text{ L/s/m}^2$. That number assumes that all gas particles arriving at the cryogenic surface are adsorbed, thus the capture probability $g = 1$. However, the cold pumping surfaces are usually thermally protected by a liquid nitrogen shroud with either louvered or chevron entrances, reducing the capture probability to 0.4 or 0.25 respectively for the two geometries. A reliable model needs to be able to predict the pumping speed based on these considerations.

The effective pumping speed relevant to testing an EP device is determined by the ratio of the flow rate from the thruster over the measured background pressure. Until recently not enough emphasis was placed on the pressure measurement methodology. High effective pumping speeds were often quoted for chambers by using pressure readings from the gauges located close to the pumping surfaces. As was discovered, these values were misleading because pressure at the thruster is often significantly higher than at the pump. More importantly the flux of particles in the chamber may not be isotropic. Studies found that the flux of particles directed at the thruster exit plane measured close to the thruster location is the most relevant parameter in determining a facility performance.²⁻⁴ The methodology of determining an effective pumping speed based on the pressure measured using an ion gauge located close to the thruster and oriented with the entrance aperture in the thrust direction is gaining a wide acceptance in the EP community.^{6,7} The second analytical model presented in this paper allows calculating the effective pumping speed based on the gauge orientation.

The rest of this paper is organized as follows. In Sec. II we describe the Node model for calculating the effective pumping speed. The Node model represents a simple application of the well-known conductance calculation for multiple pumps. In Sec. III we derive a more involved but still straightforward analytical model that is based on the particle flux balance. We compare the pumping speed estimates from both models with the measured values for two EP testing chambers in Sec. IV.

In that section we also apply both models to predict the performance of a new chamber that is currently under construction and compare the model results with a particle in cell simulation predictions. Section V summarizes salient points for both models.

II. THE NODE MODEL

The first model presented in this paper treats locations of the pumping surfaces as nodes. It computes the effective pumping speed at the thruster location P_i^{eff} due to the node i as the rated pumping speed of the node P_i adjusted for the conductance C_i between the thruster and the node locations:⁸

$$\frac{1}{P_i^{eff}} = \frac{1}{P_i} + \frac{1}{C_i} \quad (1)$$

where subscript i denotes the node index. Conductance accounts for gas interaction with the chamber surfaces and is thus a function of geometry and the gas flow. The rule for adding conductances in a complex geometry is similar to the rule of adding capacitances for an electrical circuit, while the total effective pumping speed is a linear summation of the effective pumping speed contributions from each pump⁸:

$$\frac{1}{C_{tot}} = \sum_i \frac{1}{C_i}, \quad \text{for conductances in series} \quad (2a)$$

$$C_{tot} = \sum_i C_i, \quad \text{for conductances in parallel} \quad (2b)$$

$$P^{eff} = \sum_i P_i^{eff}. \quad (2c)$$

Majority of conductance calculations relevant to the vacuum chamber geometries involve cylinders, concentric cylinders, and cones. Following Santeler's approach⁹ we calculate conductance (in L/s) as a product of the orifice conductance C_o and the transmission probability s :

$$C = sC_o, \quad (3a)$$

$$C_o = 11.43 \sqrt{\frac{T}{M}} r^2, \quad (3b)$$

$$s = \frac{1}{1 + 3l'/8r}, \quad (3c)$$

$$l' = l + \frac{l}{3 + 3l/7r}, \quad (3d)$$

where T is the gas temperature in Kelvin, M is the molecular weight of the gas, l and r are the cylinder length and radius in cm. The expressions above are valid for cylindrical tubes of circular cross-sections. These equations can be adopted for tapered and annular tubes and square cross-sections by replacing radius r in the equations above with the following expres-

sions:

$$r \rightarrow \frac{1}{2} \left[\frac{16r_1^2 r_2^2}{r_1 + r_2} \right]^{1/3} \quad \text{for tapered tube,} \quad (4a)$$

$$r \rightarrow \frac{1}{2} \left[\frac{2(r_o^2 - r_i^2)}{r_o + r_i} \right]^{1/3} \quad \text{for annular cross-section,} \quad (4b)$$

$$r \rightarrow \frac{1}{2} \left[\frac{8 a^2 b^2}{\pi a + b} \right]^{1/3} \quad \text{for square cross-section,} \quad (4c)$$

where r_o and r_i are the outer and inner radii of the annular tube and a and b are the height and width of the square cross-section.

Presence of a large cryogenic surface in a vacuum chamber may reduce the effective gas temperature below the ambient value affecting conductance. We calculate the effective gas temperature as

$$T = \frac{(1-p)T_{amb} + p(1-g)T_{cryo}}{1-pg}. \quad (5)$$

where T_{amb} is the ambient temperature (e.g. 300 K), T_{cryo} is the cryo surface temperature, and p is the probability of gas impacting on the the cryo surface and g is the capture probability.

For commercial pumps one may use the rated pumping speed for P_i in order to compute the effective pumping speed. For the custom made cryo arrays the rated pumping speed can be computed with Eq. (24).

We first illustrate the Node model with two simple examples, shown in Fig. 1. The top schematic shows a thruster installed at the left-end of a vacuum chamber that contains two pumps. The effective pumping speed of the system measured at the thruster location is computed as a sum of the effective pumping speeds due to each pump $P^{eff} = P_1^{eff} + P_2^{eff}$, where

$$\frac{1}{P_1^{eff}} = \frac{1}{P_1} + \frac{1}{C_1},$$

$$\frac{1}{P_2^{eff}} = \frac{1}{P_2} + \frac{1}{C_1} + \frac{1}{C_2}.$$

Conductances C_1 and C_2 are computed using Eq. (3) with the appropriate cross-section (if necessary using Eq. (4)) and gas temperature computed using Eq. (5).

The flexibility of the Node model is illustrated with the example shown in Fig. 1(b). Here the thruster has been moved to an appendix chamber that may have a different diameter or different cross-section than the main chamber and does not have a pump attached to it. As in the earlier example, the effective pumping speed measured at the thruster location is the sum of the effective pumping speed due to each pump in the main vacuum chamber. In this case, however, these values are

$$\frac{1}{P_1^{eff}} = \frac{1}{P_1} + \frac{1}{C_1} + \frac{1}{C_3},$$

$$\frac{1}{P_2^{eff}} = \frac{1}{P_2} + \frac{1}{C_2} + \frac{1}{C_3}.$$

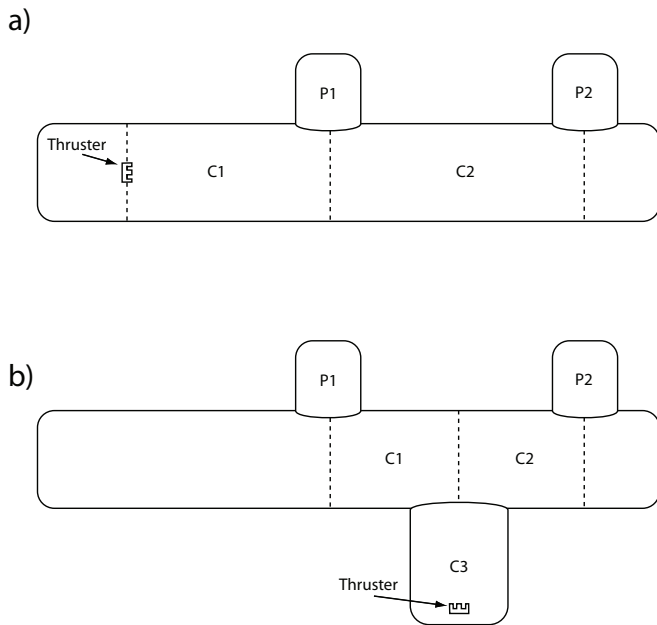


FIG. 1: Simple examples of chamber geometry used to illustrate the Node model. A thruster is located in the main vacuum chamber in pane (a), while in pane (b) the thruster is located in a cylindrical appendix attached to the main chamber.

The primary advantage of the Node model is that the pumping speed of a complex geometry may be calculated using basic spreadsheet software. The model also easily accommodates parametric optimization, with the pump or the thruster location left as a variable. For custom made cryo surfaces one can additionally optimize the temperature of the pumping surface, allowing integration of heat load requirements levied on the cryo refrigeration system. We will validate the Node model against two existing EP testing facilities at The Aerospace Corporation in Sec. IV.

III. THE FLUX MODEL

The second model is based on the gas flux balance inside a vacuum chamber. While the model can be calculated analytically, a software package capable of solving a system of linear equations would greatly speed up the process. The general approach for the model is similar to the one outlined by Cai *et al.*¹⁰ and Frieman *et al.*¹¹. Unlike the previous work however, we include some effects of the gas-wall interaction as well as a two-temperature gas flow. The biggest improvement over the earlier work lies in systematizing the approach using vector algebra and deriving flux transfer matrices for various chamber geometries. Complex geometries may thus be simulated by combining matrices and solving the resulting system of linear equations to compute gas flux and pressure at an arbitrary location. The matrix approach to determining the pumping speed of a cryopumping system has been previously proposed¹². That earlier work derived the transfer matrices based on the cryo surface locations. In that case the flux be-

tween the cryo surfaces was determined by the view factors and other geometric considerations, which made the model difficult to set up, implement, and analyze. The advantage of the current approach (and its limitation) is that the geometry is restricted to tubes and cones.

We begin developing the Flux model by noting that most of the EP testing vacuum chambers consist of cylindrical sections and end domes. An end dome section of a vacuum chamber may contain pumps and gas sources. Specifically, the flux of particles ejected from a thruster may bounce against an end dome section and thermalize. This thermal flux can be treated as a gas source at the end dome¹¹. Some of the incoming gas particles may strike the end dome wall of the chamber and assume the ambient temperature of the wall (we make an assumption of the perfect accommodation coefficient), other particles may strike a cryo pump and may not be absorbed, thus assuming the cold temperature of the cryo surface. We include both types of particle fluxes in our analysis: warm, at the chamber wall temperature, and cold, at the cold temperature of a cryo pumping surface or its shroud in cases where a relatively warm (usually LN₂) shroud surrounds a colder (usually around 20 K) pumping surface. Any two thermal fluxes that are conserved can be related through the following identity

$$n_1 v_1 = n_2 v_2 \Rightarrow n_1 \sqrt{T_1} = n_2 \sqrt{T_2} \Rightarrow n_1 = n_2 \sqrt{\frac{T_2}{T_1}} \quad (6)$$

In the following derivation of the Flux model we will define a particle density “vector” at a chamber cross-section as $\bar{n}_x = [n_{wx}^+, n_{cx}^+, n_{wx}^-, n_{cx}^-]$, where subscript x refers to the cross-section index and w and c refer to the warm and cold particles. The plus and minus superscripts refer to the flux direction, with the positive direction defined toward the right in the following drawings. Another useful identity in the derivation is the “thermal” matrix T defined as

$$T = \begin{bmatrix} 1 & \sqrt{\frac{T_c}{T_w}} & 1 & \sqrt{\frac{T_c}{T_w}} \\ \sqrt{\frac{T_w}{T_c}} & 1 & \sqrt{\frac{T_w}{T_c}} & 1 \\ 1 & \sqrt{\frac{T_c}{T_w}} & 1 & \sqrt{\frac{T_c}{T_w}} \\ \sqrt{\frac{T_w}{T_c}} & 1 & \sqrt{\frac{T_w}{T_c}} & 1 \end{bmatrix}. \quad (7)$$

A. End Dome

An end dome section can be analyzed by examining two cross-sections of the end dome that are spaced infinitely close to each other, thus allowing us to ignore the section conductance effects. Figure 2 shows a right-handed end dome configuration with warm and cold particles (subscripts w and c respectively) crossing cross-section 1 inside a vacuum chamber. Cross-section 2 was chosen to coincide with the end dome wall, thus the flux of particles moving toward the right is zero. Furthermore, a portion of the area of the end dome may be covered by a cryo pumping surface.

The probability diagram at the bottom of Fig. 2 indicates the possible scenarios for the incoming flux. A particle moving

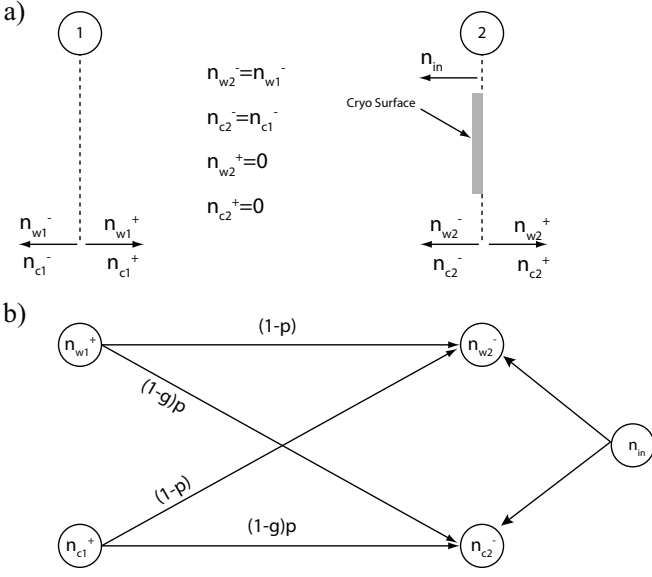


FIG. 2: Right-handed end dome. The top pane indicates fluxes at two cross-sections. The bottom pane shows potential scenarios for particle fluxes with associated probabilities.

toward the right from cross-section 1 may strike a cryo pumping surface with a probability p or the wall of the end dome with a probability $1 - p$. A particle striking the cryo surface may reflect with a probability $1 - g$, where g is the cryo pump capture probability. Thus, a warm incoming particle may reflect from the end dome section as a cold particle with the probability $(1-g)p$ and as a warm particle with the probability $1 - p$. Similar logic applies for a cold particle moving toward the right from cross-section 1. Furthermore, a source of particles at the end dome may create another contribution to the flux moving toward the left from cross-section 2. We can relate the inflow of particles with densities $[n_{w1}^+, n_{c1}^+, n_{w2}^-, n_{c2}^-]$ to the outflow of particles with densities $[n_{w2}^+, n_{c2}^+, n_{w1}^-, n_1^-]$ through a probability transfer matrix in the following way:

$$\begin{bmatrix} n_{w2}^+ \\ n_{c2}^+ \\ n_{w1}^- \\ n_{c1}^- \end{bmatrix} = \begin{bmatrix} 0 & 0 & 0 & 0 \\ 0 & 0 & 0 & 0 \\ 1-p & 1-p & 0 & 0 \\ (1-g)p & (1-g)p & 0 & 0 \end{bmatrix} \circ T \cdot \begin{bmatrix} n_{w1}^+ \\ n_{c1}^+ \\ n_{w2}^- \\ n_{c2}^- \end{bmatrix} + \begin{bmatrix} 0 \\ 0 \\ n_w^s \\ n_c^s \end{bmatrix}, \quad (8)$$

where matrix T is needed to account for the flux conservation and symbol \circ in the equation above refers to the Hadamard product¹³ where the two matrices are multiplied element-wise, i.e. for $C = A \circ B$ each element is computed as $C_{ij} = A_{ij} B_{ij}$. The first two rows of the probability transfer matrix express the boundary condition of no flux out of the vacuum chamber ($n_{w2}^+ = n_{c2}^+ = 0$). The assumption of the infinite closeness of the two cross-sections allows us to ignore the conductance effects in the end dome section, and thus using the equality of the left-going fluxes ($n_{w2}^- = n_{w1}^-$ and $n_{c2}^- = n_{c1}^-$) we can rewrite Eq. (8) as a boundary condition

$$\begin{bmatrix} n_{w1}^+ \\ n_{c1}^+ \\ n_{w1}^- \\ n_{c1}^- \end{bmatrix} = \begin{bmatrix} 1 & 0 & 0 & 0 \\ 0 & 1 & 0 & 0 \\ 1-p & 1-p & 0 & 0 \\ (1-g)p & (1-g)p & 0 & 0 \end{bmatrix} \circ T \cdot \begin{bmatrix} n_{w1}^+ \\ n_{c1}^+ \\ n_{w1}^- \\ n_{c1}^- \end{bmatrix} + \begin{bmatrix} 0 \\ 0 \\ n_w^s \\ n_c^s \end{bmatrix}, \quad (9)$$

where now the first two rows of the probability transfer matrix state the identity relationship for the warm and cold right-moving fluxes and the bottom two rows determine the probabilities of the fluxes reflecting from the end dome surface. The right-handed boundary condition can now be written in the matrix notation as

$$\bar{n}_1 = R \cdot \bar{n}_1 + \bar{n}_{RB}^s, \quad (10)$$

where $\bar{n}_1 = [n_{w1}^+, n_{c1}^+, n_{w1}^-, n_{c1}^-]$, $\bar{n}_{RB}^s = [0, 0, n_w^s, n_c^s]$ and the flux transfer matrix R is defined as

$$R = \begin{bmatrix} 1 & 0 & 0 & 0 \\ 0 & 1 & 0 & 0 \\ 1-p & 1-p & 0 & 0 \\ (1-g)p & (1-g)p & 0 & 0 \end{bmatrix} \circ T. \quad (11)$$

Using similar arguments we can show that the left-handed boundary condition can be written as

$$\bar{n}_1 = L \cdot \bar{n}_1 + \bar{n}_{LB}^s, \quad (12)$$

where $\bar{n}_{LB}^s = [n_w^s, n_c^s, 0, 0]$ and the flux transfer matrix L is defined as

$$L = \begin{bmatrix} 0 & 0 & 1-p & 1-p \\ 0 & 0 & (1-g)p & (1-g)p \\ 0 & 0 & 1 & 0 \\ 0 & 0 & 0 & 1 \end{bmatrix} \circ T. \quad (13)$$

B. Cylindrical Section

Deriving the flux transfer matrix for the cylindrical section with a pump is more challenging because a path that a particle takes while traversing the section may contain infinite chain of events, such as a collision with a wall or a pump and absorption by the cryo surface. In order to make the derivation tractable we assume that all collisions with the wall or the pump occur in the middle of the cylindrical section.

In addition to the probabilities p and g defined in the previous section, we also need to define the probability for a particle to transit through the section without striking the wall c and the overall probability of transition to the opposite side of the section – the Santeler's probability s ⁹. The transition probability c is needed for the particles whose temperature is different than the chamber wall temperature, while the Santeler's probability is used when the gas and the wall temperatures are equal. The Santeler's probability is defined by Eqs. 3(c) and 3(d) as a function of the section's length l and its diameter d . In some custom-made vacuum chambers the cryopumping surfaces may protrude significantly from the chamber wall or be located inside the chamber, thus invalidating the use of the Santeler's probability in the Flux model. We will ignore this effect because such configurations require recalculation of the probability s and do not lend well to a generic analysis.

The probability of a particle transiting a section without striking the wall can be determined using a Monte Carlo simulation. We simulated 1000 particles that were homogeneously distributed at one end of a cylinder at the beginning of the simulation and were allowed to propagate according to a randomly selected velocity in three dimensions. The velocity

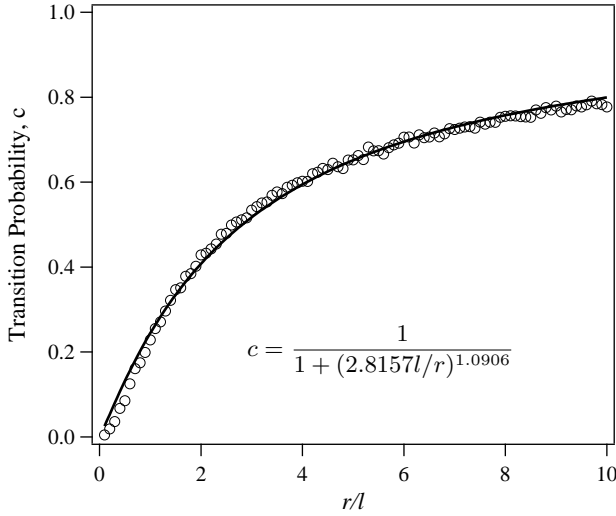


FIG. 3: Transition probability for a cylindrical section of length l and diameter d . The open circles represent the results of multiple Monte-Carlo simulations, while the solid curve is a Hill equation fit to the simulation data.

was selected in accordance with the thermal distribution corresponding to the temperature T of the gas. The particles that impinged on the chamber wall were removed from the simulation. The transition probability c was computed as a ratio of the number of particles that reached the opposite side of the section without striking the wall to the initial number of particles entering the section. We performed multiple simulations with a range of gas temperatures and section lengths and diameters. We found that the results did not depend on the gas temperature, as expected for a non-collisional particle distribution. Furthermore, when plotted against the aspect ratio r/l the simulation results collapsed to a single curve, shown in Fig. 3. The curve was fitted with the Hill equation¹⁴

$$c = b + \frac{m - b}{1 + (\Delta \frac{l}{r})^a}$$

while forcing $b = 0$ and $m = 1$ to ensure that the probability is zero when $r/l = 0$ and is one when $r/l \rightarrow \infty$. The best fit was obtained with $\Delta = 2.8157$ and $a = 1.0906$.

With the four probabilities ($p, g, s,$ and c) defined we can now derive the flux transfer matrix. Figure 4 shows a schematic of a section with the corresponding probability diagrams below it. The strategy for deriving the flux transfer matrix is to first write down a matrix that maps the flux of particles into the control volume onto the flux of particles leaving it from both ends. Then, we manipulate the resulting matrix to map the flux of particles through the boundary 1 onto the flux of particles through the boundary 2.

The first probability diagram (pane b) shows the probability chains for the warm gas moving in the positive direction (toward the right of the figure) through the boundary 1, n_{w1}^+ . A particle can either strike the pump with a probability p , transit to the boundary 2 with a probability $(1-p)s$, or come back

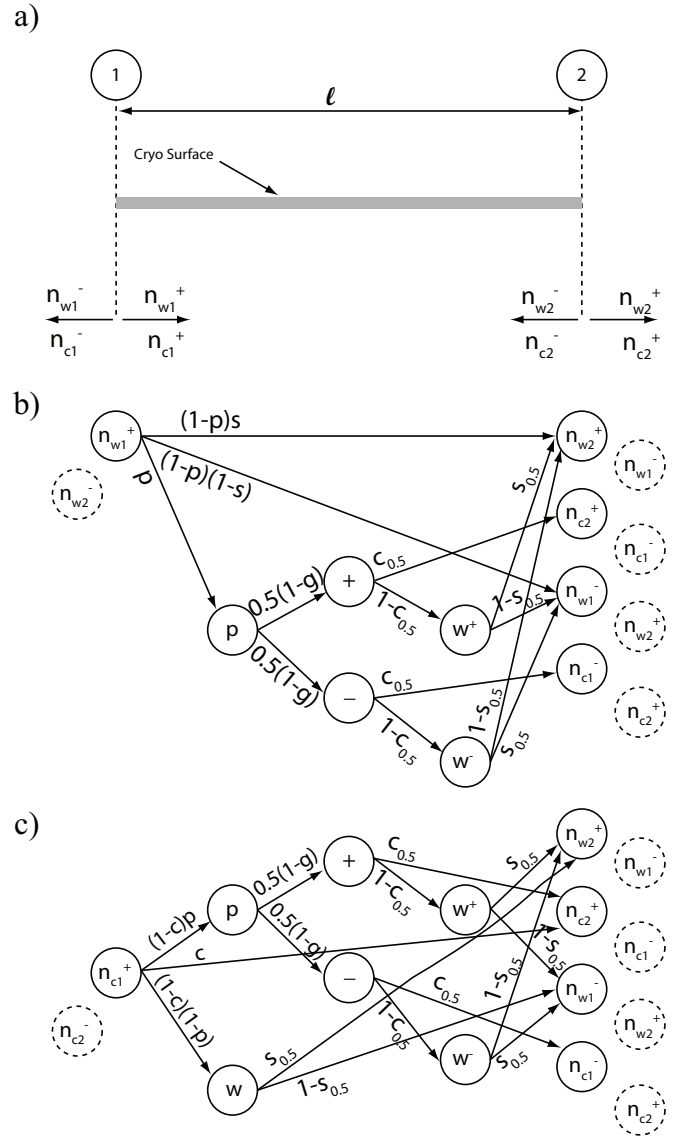


FIG. 4: Schematic of a chamber section with a pump showing the fluxes at the two cross-sections. The probability diagrams below the schematic outline the probability chains for the right-moving warm particles (top pane) and cold particles (bottom pane). The probability chains for the left-moving particles are obtained by substituting the included dashed spheres with the included dashed spheres, as appropriate.

to the boundary 1 with a probability $(1-p)(1-s)$ after colliding with the wall. There is a probability g that a particle that strikes a pump will be adsorbed (pumped) or probability $0.5(1-g)$ that the particle will not be adsorbed and reflect in either the positive or negative direction. That particle, moving in either direction, can then either transit the chamber with a probability $c_{0.5}$ without colliding with the wall or collide with the wall with a probability $(1-c_{0.5})$. The subscript “0.5” in the transit probability implies that we compute this probability with $0.5l$ instead of l , assuming that the collision occurred in the middle of the chamber. Finally, the particle that was scattered by the pump and then collided with the wall can ei-

ther traverse the rest of the chamber with a probability $s_{0.5}$ or reverse the direction and exit on the opposite end with a probability $1 - s_{0.5}$. Here again subscript “0.5” refers to the Santeler’s probability calculated from the middle of the section. Similar logic applies to a warm particle moving in the negative direction through the boundary 2 (n_{w2}^-), as indicated by the dashed circles in the top probability diagram of Fig. 4.

The probability diagram for a cold particle is shown on the bottom of Fig. 4. Here a cold particle moving in the positive direction through the boundary 1 can either transit the section with a probability c without striking the wall or the pump, strike the pump with a probability $(1 - c)p$, or strike the wall with a probability $(1 - c)(1 - p)$. After a wall collision, the particle can either continue in the same direction to exit at the boundary 2 with a probability $s_{0.5}$ or reverse the direction and exit the section at the boundary 1 with a probability $1 - s_{0.5}$. After a pump collision we can apply the same logic as we used for the warm particles in the paragraph above. Finally, a similar probability diagram can be drawn for a cold particle moving in the negative direction through the boundary 2 (n_{c2}^-), as indicated by the dashed circles in the bottom probability diagram of Fig. 4.

The probability transfer matrix B connects the input flux vector $[n_{w1}^+, n_{c1}^+, n_{w2}^-, n_{c2}^-]$ with the output flux vector $[n_{w2}^+, n_{c2}^+, n_{w1}^-, n_1^-]$ such that

$$\begin{matrix} n_2^+ \\ n_1^- \end{matrix} \left\{ \begin{matrix} [n_{w2}^+ \\ n_{c2}^+ \\ n_{w1}^- \\ n_{c1}^-] \end{matrix} \right\} = \begin{bmatrix} B_d & B_s \\ B_s & B_d \end{bmatrix} \circ T \cdot \begin{matrix} n_1^+ \\ n_2^- \end{matrix} \left\{ \begin{matrix} [n_{w1}^+ \\ n_{c1}^+ \\ n_{w2}^- \\ n_{c2}^-] \end{matrix} \right\} \quad (14)$$

where B_d and B_s are 2×2 matrices

$$B_d = \begin{bmatrix} (1-p)s & (1-p)(1-c)s_{0.5} \\ +0.5p(1-g)(1-c_{0.5}) & +0.5p(1-g)(1-c)(1-c_{0.5}) \\ 0.5p(1-g)c_{0.5} & c + 0.5p(1-g)(1-c)c_{0.5} \end{bmatrix}, \quad (15)$$

$$B_s = \begin{bmatrix} (1-p)(1-s) & (1-p)(1-c)(1-s_{0.5}) \\ +0.5p(1-g)(1-c_{0.5}) & +0.5p(1-g)(1-c)(1-c_{0.5}) \\ 0.5p(1-g)c_{0.5} & 0.5p(1-g)(1-c)c_{0.5} \end{bmatrix}.$$

The T matrix is needed in order to maintain flux conservation, just like in the end dome calculation. As the final step in the derivation of the flux transfer matrix we rewrite Eq. (14) as a set of linear equations, which we solve for the flux through the boundary 2 $[n_2^+, n_2^-]$ as a function of the flux through the boundary 1 $[n_1^+, n_1^-]$. The system of linear equations corresponding to Eq. (14) is

$$\begin{aligned} n_2^+ &= B_d \cdot n_1^+ + B_s \cdot n_2^- \\ n_1^- &= B_s \cdot n_1^+ + B_d \cdot n_2^- \end{aligned} \quad (16)$$

where we have omitted the terms of the T matrix, as they can be added later without invalidating the derivation. The system above can be solved to produce

$$\bar{n}_2 = C \cdot \bar{n}_1, \quad (17)$$

where $\bar{n}_x = [n_{wx}^+, n_{cx}^+, n_{wx}^-, n_{cx}^-]$ is the flux vector through the boundary x in both directions. The flux matrix C is de-

finied as

$$C = \begin{bmatrix} B_d - B_s \cdot B_d^{-1} \cdot B_s & B_s \cdot B_d^{-1} \\ -B_d^{-1} \cdot B_s & B_d^{-1} \end{bmatrix} \circ T \quad (18)$$

A source term can be added to Eq. (17), similarly to Eqs. (10) and (12). We will show an example of such a case in the next section. While matrix C may look complicated, once the four probabilities are determined, the matrix becomes a straight-forward numerical 4×4 matrix, which can be easily used to solve for the fluxes.

Unlike the Node model, the Flux model requires the pressure gauge position and orientation in order to convert fluxes into pressure. The pumping speed of a vacuum facility is defined as the ratio of the source fluxes over the particle density as measured by a pressure gauge per unit area:

$$P^{eff} = \frac{n^s \sqrt{\frac{k_b T_w}{2\pi m}}}{A n_g}, \quad (19)$$

where we assumed that the gas source is warm and that n_g is the particle density inside the pressure gauge and is computed as

$$n_g = \sqrt{\frac{T_w}{T_g}} n_{wx} + \sqrt{\frac{T_c}{T_g}} n_{cx}, \quad (20)$$

where n_{wx} and n_{cx} are the warm and cold particle densities through the boundary x where the ion gauge is located in the direction toward the gauge opening, and T_g is the temperature of the gauge cavity. Equations (10), (12), (17), and (19) with the appropriate definitions of the four probabilities (p , g , c , and s) for each chamber section and the boundary conditions are all that is necessary to construct the Flux model for a vacuum chamber.

C. Ideal Pumping Speed of an Infinite Cryo Surface

A simple example can serve as a useful exercise and to demonstrate the utility of the Flux model. We consider a short cylindrical section of a large radius without pumps connected to the end domes on either side, as shown in Fig. 5. The surface of the right-end dome is maintained at a cold temperature, which provides cryopumping, while the opposite end dome is maintained at a warm temperature and serves as a gas source. The right-end dome evaporates a small amount of gas that contributes n_v to the gas density. We can treat the evaporating gas as a source term at the right boundary. The set of equations describing the the system is

$$\begin{aligned} \bar{n}_1 &= L \cdot \bar{n}_1 + \bar{n}^s \\ \bar{n}_2 &= C \cdot \bar{n}_1 \\ \bar{n}_2 &= R \cdot \bar{n}_2 + \bar{n}^v, \end{aligned} \quad (21)$$

where $\bar{n}^s = [n_s, 0, 0, 0]$ and $\bar{n}^v = [0, 0, n_v, 0]$. We can combine the three equations above to solve for \bar{n}_1 :

$$\bar{n}_1 = L \cdot C^{-1} \cdot R \cdot C \cdot \bar{n}_1 + L \cdot C^{-1} \cdot \bar{n}^v + \bar{n}^s \quad (22)$$

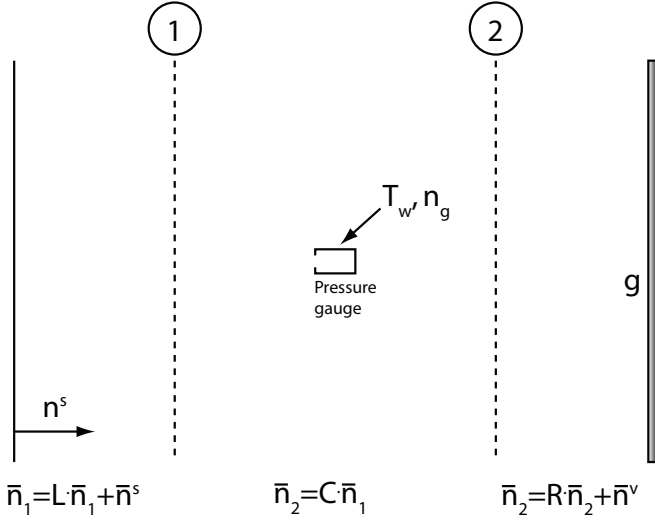


FIG. 5: Schematic showing infinite parallel plates connected by a cylindrical section. A warm gas source is located at the left wall, while the right wall is at sufficiently cold temperature to pump the gas.

If we assume that the radius of the system is sufficiently large to be treated as infinite and since the cylindrical section does not contain a pump the four probabilities of the flux matrix C are $p = 0, g = 0, c = 1$, and $s = 1$, which reduces it to the identity matrix. For the right-hand boundary condition we also have $p = 1$ while g is left as a parameter. There isn't a cryo surface on the left-end dome, so $p = g = 0$. With these parameters Eq. (22) reduces to the following set of linear equations

$$n_{w1}^+ = (1 - g)n_{w1}^+ + \sqrt{\frac{T_c}{T_w}}gn_v + n_s \quad (23a)$$

$$n_{c1}^+ = 0 \quad (23b)$$

$$n_{w1}^- = 0 \quad (23c)$$

$$n_{c1}^- = \sqrt{\frac{T_w}{T_c}}(1 - g)n_{w1}^+ + gn_v. \quad (23d)$$

Equations 23(b) and (c) state that there is no flow of cold particles in the positive direction and no flow of warm particles in the negative direction across boundary 1, as expected. With a pressure gauge oriented to measure the flux of warm particles, as shown in Fig. 5, and also assuming that the gauge is at the warm temperature T_w , the density inside the gauge equals n_{w1}^+ (using momentum conservation in and out of the gauge).

Solving 23(a) for the source density n_s and substituting the ideal equation of state for the evaporation density ($P_v = n_v k_b T_c$) and the warm particle density ($P_w = n_{w1}^+ k_b T_w$) we can derive the pumping speed, which is given as the ratio of the ‘‘throughput of the system divided by the pressure measured at the point at which the pumping speed is defined’’, or equivalently the input flux divided by the density at the pres-

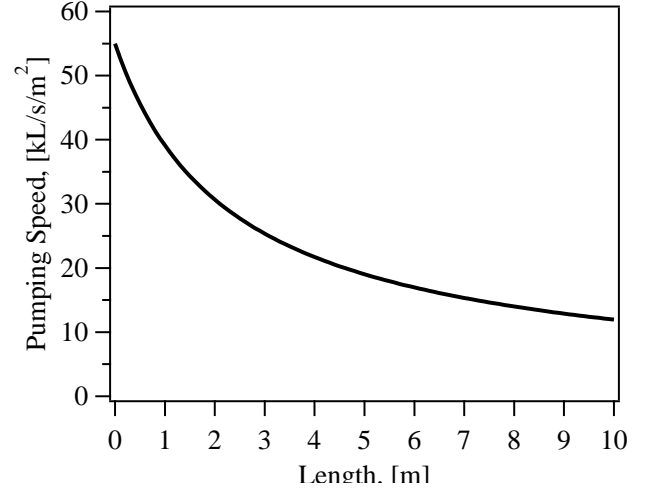


FIG. 6: Pumping speed as a function of the distance separating two finite parallel plates. The chamber radius of 1.2 m was assumed in the calculations.

sure gauge, as

$$P = A \frac{n_s v_s / 4}{n_g} = Ag \frac{v_s}{4} \frac{n_{w1}^+ - \sqrt{\frac{T_c}{T_w}} n_v}{n_{w1}^+} \quad (24)$$

$$= Ag \sqrt{\frac{k_b T_w}{2\pi m}} \left[1 - \frac{P_v}{P} \sqrt{\frac{T_w}{T_c}} \right].$$

where A is the cryo array surface area and P_v is the vapor pressure of the gas. For xenon Eq. (24) gives the maximum pumping speed (assuming $g = 1$, and $P_v = 0$) of 54,975 L/s per m^2 of the cryopumping area, which is the number used in Ref. [15]. If we assume that the system has a finite radius, the conductance losses will decrease the pumping speed because probabilities s and c decrease as a function of length. This dependence is shown in Fig. 6, where we assumed a radius of 1.2 meters. In order to obtain the curve shown in the figure we solved Eq. (22) for multiple values of spacing between the end domes.

IV. MODEL APPLICATIONS

In this section we use the Node and the Flux models to analyze two electric propulsion testing facilities at The Aerospace Corporation. The two facilities have sufficiently different configurations to demonstrate the flexibility of both models. Furthermore, we use the Node and Flux models to analyze a new facility, which is currently being designed.

A. EP2

The first facility that we analyze is the EP2 vacuum chamber^{2,16}. The chamber is roughly 2.4 m in diameter and 10 m long. It is pumped by 10 PHPK TM-1200 cryopumps,

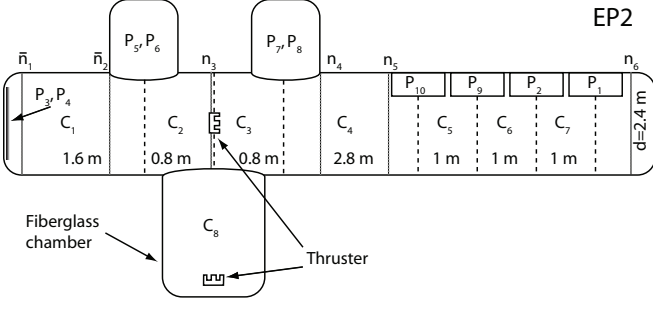


FIG. 7: Schematic of the EP2 chamber. The black dashed lines are used to identify distances for the Node model computation, while the gray dashed lines are used to identify the sections for the Flux model.

as shown in Fig. 7. Two re-entrant cryopanel, labeled P_3 and P_4 are located at the left-end dome of the tank. Four other re-entrant cryopumps are arranged sequentially next to the right-end dome and are labeled P_1 , P_2 , P_9 , and P_{10} , as shown. Finally, two cryotubs, labeled P_5 and P_6 are located 1.6 m from the left-end dome and two more cryotubs, labeled P_7 and P_8 are located 3.2 m from the left-end dome. The re-entrant cryopumps have the rated pumping speed of 35 kL/s on xenon, while the cryotubs have the rated pumping speed of 25 kL/s on xenon. We note that the quoted distances and dimensions are approximate, but sufficiently accurate for the current calculation.

One of the unique features of the EP2 chamber is the 0.9 m diameter, 1.5 m long fiberglass chamber appendix that enables the Electromagnetic Interference and Compatibility (EMI/EMC) testing of the EP devices. The fiberglass chamber is connected to the main chamber through a gate valve, thus a thruster may be located in the main chamber for performance and plume measurements or in the fiberglass chamber for the EMI measurements, as indicated in Fig. 7.

During experiments the pumping speed is computed using pressure measured by an ion gauge located within 10 cm of the thruster, placed on a T with an opening in the direction of the thruster plume exhaust, in a configuration adopted from Ref. [4]. Pumping speed as a function of the number of active pumps is shown by open circles in Fig. 8. The label next to each data point indicates the identity of the active pumps. For example, cryotub #7 (P_7 in Fig. 7) was used when only one pump was active.

The Node model for the main chamber (without including the fiberglass appendix) can be computed as a sum of the pumping speed contributions of the ten pumps determined at the thruster location:

$$P^{eff} = \sum_{i=1,2,9,10} P_i^{eff} + P_{3,4}^{eff} + P_{5,6}^{eff} + P_{7,8}^{eff}$$

$$1/P_{3,4}^{eff} = 1/(P_3 + P_4) + \sum_{i=1,2} 1/C_i$$

$$1/P_{5,6}^{eff} = 1/(P_5 + P_6) + 1/C_2$$

$$1/P_{7,8}^{eff} = 1/(P_7 + P_8) + 1/C_3$$

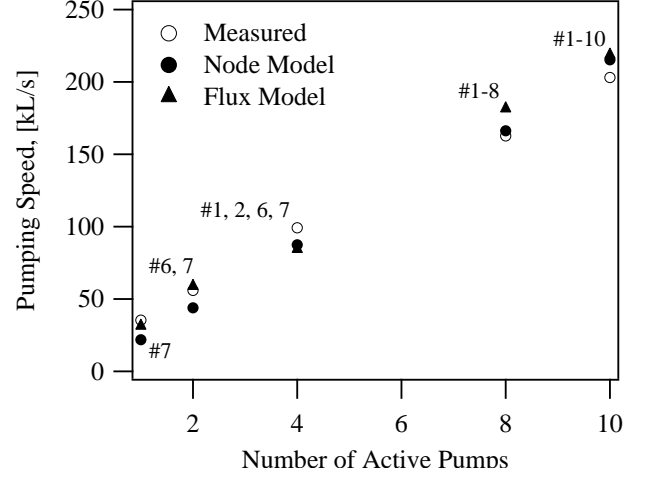


FIG. 8: Pumping speed of the EP2 chamber as a function of the number of active pumps. The pump identity is noted for each data point

$$\begin{aligned} 1/P_{10}^{eff} &= 1/P_{10} + \sum_{i=3,4} 1/C_i \\ 1/P_9^{eff} &= 1/P_9 + \sum_{i=3-5} 1/C_i \\ 1/P_2^{eff} &= 1/P_2 + \sum_{i=3-6} 1/C_i \\ 1/P_1^{eff} &= 1/P_1 + \sum_{i=3-7} 1/C_i \end{aligned} \quad (25)$$

We note that a “reduced” radius was used in order to calculate conductances C_5 , C_6 , and C_7 in order to account for the partial blockage of the chamber by the re-entrant pumps 1, 2, 9, and 10. Pumping speed at the thruster location as a function of the number of active pumps can be computed by zeroing out the appropriate values of P_i . Results of such a computation show a good agreement with the experimentally derived pumping speed, as shown in Fig. 8, where the Node model is indicated by the closed circles. We note that for this comparison the identity of the active pumps matched the experimental setup.

In order to compute the effective pumping speed measured at the thruster, when it is located in the fiberglass chamber, we need to adjust each line of Eq. (25) to include conductance C_8 . For brevity, we will not write down the resulting set of equations, but note that the effective pumping speed computed inside the fiberglass chamber with all 10 cryopumps active is 64.5 kL/s, which is about a third of the pumping speed measured with the thruster in the main chamber. That value is consistent with the reported pressure values in the fiberglass chamber.⁵

We construct the Flux model for EP2 using five cylindrical sections outlined by the gray dashed lines in Fig. 7, with the first four labeled by C_1 , C_2 , C_3 , and C_4 . The last cylindrical section is a combination of the sections labeled C_5 , C_6 , and C_7 with a total pumping speed corresponding to the sum of pumps P_{10} , P_9 , P_1 and P_2 – that combined section is referred

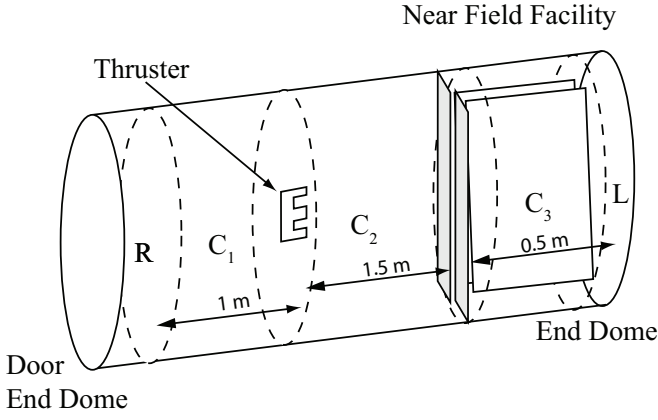


FIG. 9: Schematic of the Near Field Facility.

as C_5 in the following discussion. A more accurate model can be constructed by treating each pump and each section separately, but as we shall see, this simplification still produces a good agreement with the measurements. The left-end dome is partially covered by cryopumps and has no gas sources. The right-end dome, on the other hand, has no pumps but is treated as having a gas source. The gas source is produced by the thruster plume that impinges and thermalizes on the right-end dome. The resulting set of equations that define the Flux model for EP2 is

$$\begin{aligned}
 \bar{n}_1 &= L \cdot \bar{n}_1 & \bar{n}_2 &= C_1 \cdot \bar{n}_1 \\
 \bar{n}_3 &= C_2 \cdot \bar{n}_2 & \bar{n}_4 &= C_3 \cdot \bar{n}_3 \\
 \bar{n}_5 &= C_4 \cdot \bar{n}_4 & \bar{n}_6 &= C_5 \cdot \bar{n}_5 \\
 \bar{n}_6 &= R \cdot n_6 + \bar{n}_{in},
 \end{aligned} \tag{26}$$

where $\bar{n}_{in} = [0, 0, n_s, 0]$ and the location at which we measure fluxes \bar{n}_1 through \bar{n}_6 is as indicated in Fig. 7. The equations above can be combined to solve for the flux at the thruster location \bar{n}_3

$$\begin{aligned}
 C_5 \cdot C_4 \cdot C_3 \cdot \bar{n}_3 &= \\
 = R \cdot C_5 \cdot C_4 \cdot C_3 \cdot C_2 \cdot C_1 \cdot L \cdot C_1^{-1} \cdot C_2^{-1} \bar{n}_3 + \bar{n}_{in}.
 \end{aligned} \tag{27}$$

The pumping speed at the thruster is computed similarly to Eq. (24)

$$P = A \frac{n_s v_s / 4}{n_{w3}^- + \sqrt{\frac{T_c}{T_w}} n_{c3}^-}, \tag{28}$$

where $A = \pi r^2$ is the area of the chamber cross-section. We note that the denominator in the equation above takes into account fluxes of both warm n_{w3}^- and cold n_{c3}^- particles contributing to the gauge density n_g . In order to compute Eq. (27) we assume that $T_w = 300$ K, $T_c = 90$ K. The front of the PHPK TM-1200 pumps contains LN2 cooled louvers, which protect the helium cooled inner sail of the pumps.¹⁷ We thus chose capture probability $g = 0.4$ to correspond to the louvered geometry.⁸ This assumption is consistent with the results obtained in Refs. [10] and [11]. The pumping speed

computed with the Flux model for EP2 is shown for the same combination of active pumps as measured in Fig. 8. Just like the Node model, the Flux model shows a good agreement with the experimentally measured pumping speed.

B. The Near Field Facility (NFF)

The Near Field Facility (NFF) at The Aerospace Corporation has been used for diagnostic development¹⁸ and small thruster characterization¹⁹. The facility comprises a 3 m long and 1.5 m diameter stainless steel chamber, shown schematically in Fig. 9. The chamber is pumped by two 0.9 m by 0.5 m He-cooled nude sails, which are cooled to 15 K by two CVI CBST 6.0 compressors. A liquid nitrogen shroud envelops the entire cylindrical portion of the chamber and the end dome (on the left of the schematic), while multi-layered insulation covers the door (on the right of the schematic). Two copper panels, cooled by liquid nitrogen, are installed in front of the He sails. The copper panels are designed to screen the sails from the thruster beam. The side of the panels facing the thruster is covered with carbon felt to reduce sputtering. Carbon felt is also used on a circular panel covering the right-end dome of the chamber. Multiple thermocouples indicate that the temperature of the LN2 shroud and the copper panels range between 90 K and 120 K.

The Node model for the NFF chamber is particularly simple and consists of two sections indicated by C_2 and C_3 in Fig. 9. We calculate the pumping speed of the nude sails P_s using Eq. (24) and conductance C of the cylindrical span between the thruster location and the center of the nude sails (1.75 m) using Eq. (3). One remaining unknown in Eq. (24) is the capture probability g , which cannot be measured directly. The capture probability is a product of the sticking coefficient, which is the probability of a particle adsorbing to a surface and a view factor, which is the probability of a particle getting to the surface. For the nude sails the view factor for the sail surfaces facing the chamber walls is assumed to be unity, however the view factor for the inner-facing surfaces cannot be easily estimated. Furthermore, the sticking coefficient cannot be measured directly either. We therefore compute the pumping speed for three values of capture probability $g = 0.25, 0.5$ and 0.85 which should bound the pumping speed estimation. The Node model equation is

$$P(T) = \frac{P_s(T) + C(T)}{P_s(T)C(T)}, \tag{29}$$

where we left gas temperature as a variable. The gas temperature inside the NFF is determined by the wall temperature, which varies between 90 and 120 K. If the accommodation coefficient (which is defined by the thermal transfer between the wall and the impinging gas) is not unity the gas temperature may be higher than the wall temperature. Pumping speed estimation from the Node model as a function of gas temperature is shown in Fig. 10 with solid black curves for three values of g . The hashed box in the figure indicates the range of the measured chamber wall temperatures and pumping speeds. The

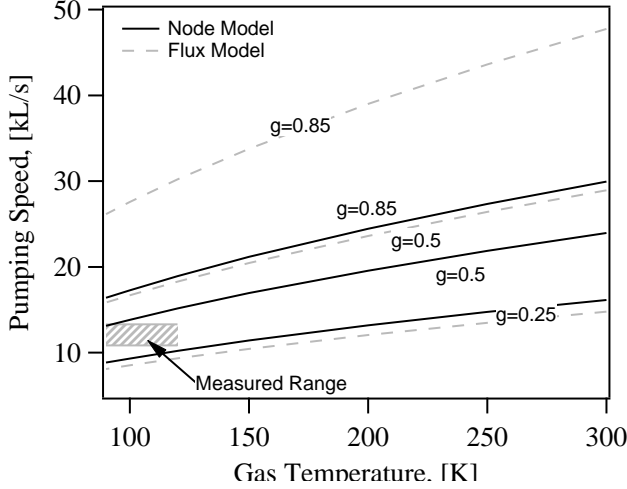


FIG. 10: Pumping speed as a function of the gas temperature in the NFF. The dashed area indicates measured pumping speed and LN2 shroud temperature ranges.

results indicate that the capture probability for the sails in the NFF system is between 0.3 and 0.5.

The Flux model for the NFF chamber can be constructed using three cylindrical sections, as indicated in Fig. 9. The space between the chamber door and the cryo sails is split into two sections (section 1 and 2) in order to define the thruster location at the boundary between the two sections. These two sections have no pumps and thus $p = g = 0$. The third section contains the cryo sails. The probability of gas impinging on the sails p is defined as the ratio between the total sail area and the chamber wall area. Additionally, to account for the reduction in the view factor of the inner-facing surfaces of the sails, we reduce the “effective” inner area by a factor of 2. This is an arbitrary assumption in lieu of a more careful analysis, which is required for a higher fidelity simulation. The set of equations that describes the Flux model for the NFF is

$$\begin{aligned} \bar{n}_1 &= L \cdot \bar{n}_1 & \bar{n}_2 &= C_1 \cdot \bar{n}_1 \\ \bar{n}_3 + \bar{n}_3^s &= C_2 \cdot \bar{n}_2 & \bar{n}_4 &= C_3 \cdot \bar{n}_3 \\ \bar{n}_4 &= R \cdot \bar{n}_4. \end{aligned} \quad (30)$$

In the equation set above we make a conservative assumption that all of the thruster plume scatters from the LN2 cooled, felt-covered copper panels that screen the cryo sails and thus introduced a source term $\bar{n}_3^s = [0, 0, n_s, 0]$ in the second cylindrical section. Allowing a part of the plume to scatter off the right-end dome should increase the calculated pumping speed. We can solve the system of equations above for the fluxes at the thruster location \bar{n}_2

$$\begin{aligned} C_3 \cdot C_2 \cdot n_2 &= \\ &= R \cdot C_3 \cdot C_2 \cdot C_1 \cdot L \cdot C_1^{-1} \cdot n_2 + (I - R) \cdot C_3 \cdot n_3^s \end{aligned} \quad (31)$$

and then calculate the pumping speed at the thruster location using Eq. (28) with $\bar{n}_{w2,c2}$ substituted for $\bar{n}_{w3,c3}$. In the above

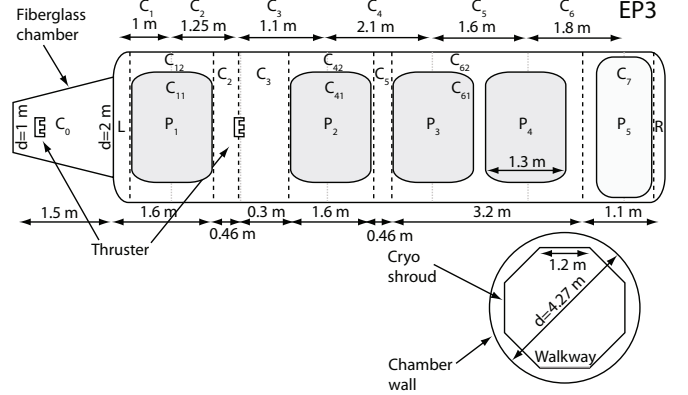


FIG. 11: Schematic of the EP3 vacuum chamber. Pumps P_1 through P_4 are custom-made cryo surfaces, while P_5 consists of 6 PHPK TM-1200i cryopumps arranged in a ring configuration.

equation I is the identity matrix. The Flux model predictions for the pumping speed as a function of gas temperature are shown by gray dashed curves in Fig. 10. The curves with the capture probability of 0.25 show a good agreement with the Node model results, however with a higher capture probability the Flux model predicts a higher pumping speed for a given gas temperature. When compared to the measured pumping speed and cryo shroud temperature of the chamber both models indicate that the capture probability of the cryo sails is between 0.3 and 0.5.

C. EP3

As a final example we apply both models to predict the pumping speed of the new EP3 facility. The new vacuum chamber is designed as a 4.27 m diameter, 10 m long metal cylinder with a conical fiberglass antechamber connected to the main chamber, as shown in Fig. 11. The pumping system consists of four custom made helium cooled cryo ring assemblies, indicated as P_1, P_2, P_3 and P_4 in Fig. 11 and six PHPK TM-1200i reentrant cryopumps arranged in a ring configuration next to the chamber door and indicated as P_5 . Each cryo ring consists of seven cryo panels arranged in the octagonal configuration with the bottom panel absent to accommodate a walkway. Each cryo panel is approximately 1.3 m long (along the vacuum chamber cord) and 1.2 m wide (along the chamber circumference). Additionally, each helium cooled panel is sandwiched between two LN2 cooled surfaces. The inner LN2 surface has louvered openings to allow gas penetration to the helium surface. Finally, a radiation shield is added to each panel as the outermost surface. We will ignore the radiation shield as it does not have a significant effect on the pumping speed calculation. The ring configuration was optimized to allow significant pumping both on the front and the back surfaces of the helium cooled panel. Therefore, in or-

der to calculate the total pumping speed we need to take into account conductance in the core of the chamber as well as in the annular region between the helium panels and the chamber wall.

A thruster can be placed in two locations within the chamber. The first location is between the first and second cryo rings, and the second location is in the back of the fiberglass antechamber, as shown in Fig. 11. We will derive the Node and Flux models for the thruster located in the main chamber, and for brevity will only provide the final results for the pumping speed with the thruster in the fiberglass antechamber. The Node model is calculated using the effective pumping speed in the core of the chamber, defined as the space from the centerline to the cryo rings, and the annular region, between the cryo rings and the chamber wall. The effective pumping speed of the chamber core is

$$\begin{aligned}
P_{core}^{eff} &= \sum_{i=1-5} P_i^{eff} \\
1/P_1^{eff} &= 1/P_1 + 1/C_2 \\
1/P_2^{eff} &= 1/P_2 + 1/C_3 \\
1/P_3^{eff} &= 1/P_3 + \sum_{i=3,4} 1/C_i \\
1/P_4^{eff} &= 1/P_4 + \sum_{i=3-5} 1/C_i \\
1/P_5^{eff} &= 1/P_5 + \sum_{i=3-6} 1/C_i,
\end{aligned} \tag{32}$$

where conductances C_i are calculated using the distance from the thruster to the center of the pumping surface i , locations shown by the gray dashed lines in Fig. 11. The effective pumping speed in the annular region of the chamber P_{ann}^{eff} can be computed using a similar set of equations with the conductances computed with the adjusted radius, as described by Eq. (4)(b), and with one additional conductance, accounting for the gas path from the core to the annular region of the chamber, added to every equation above. We also note that pumping speed for P_1 through P_4 are computed using equation Eq. (24) with $g = 0.4$ for the P_{core}^{eff} to account for the louvers on the inner facing surfaces and with $g = 0.85$ for the outer facing surfaces. The overall pumping speed of the system is $P^{eff} = P_{core}^{eff} + P_{ann}^{eff}$. The Node model estimates 700,570 L/s as the pumping speed measured at the thruster. In this case the Node model provides a conservative estimate since it does not include all possible paths for the gas to reach the pumping surfaces. The contributions of the individual cryo-rings and the pumps are shown in Table I. The table shows that ring 2 provides the greatest contribution to the overall pumping speed – this is expected, as ring 2 is located immediately downstream of the thruster. The table also lists the pumping speed contributions of the back side (outward facing surfaces) of each of the four cryo-rings. The Node model predicts that the cryo-ring back surfaces provide $\sim 45\%$ of the overall pumping capacity. When a thruster is installed in the fiberglass antechamber the Node model predicts 324,473 L/s measured at the thruster location.

The Flux model is constructed by dividing the chamber into

Pumping speed, [L/s]	Ring 1	Ring 2	Ring 3	Ring 4	Pumps
Total	184,010	195,248	149,089	113,325	58,897
Node Model	Back 91,946	101,429	73,988	47,968	
Flux Model	Total 186,617	234,296	442,664	183,638	
	Back 63,607	136,515	204,888		

TABLE I: EP3 pumping speed breakdown by pumping the elements.

7 cylindrical sections. Section 6 contains cryo-rings P_3 and P_4 because these two rings are immediately adjacent and can be treated as one cryo surface. Sections containing the cryo-rings are separated into the core (C_{11} , C_{41} , and C_{61}) and annular (C_{12} , C_{42} , and C_{62}) regions. The Flux model for the chamber can be written as

$$\begin{aligned}
\bar{n}_1 &= L \cdot \bar{n}_1 & \bar{n}_{11} &= \frac{s_{11}}{s_{11} + s_{12}} \bar{n}_1 \\
\bar{n}_2 &= C_{11} \cdot \bar{n}_{11} + C_{12} \cdot \bar{n}_{12} & \bar{n}_{12} &= \frac{s_{12}}{s_{11} + s_{12}} \bar{n}_1 \\
\bar{n}_3 &= C_2 \cdot \bar{n}_2 \\
\bar{n}_4 &= C_3 \cdot \bar{n}_3 & \bar{n}_{41} &= \frac{s_{41}}{s_{41} + s_{42}} \bar{n}_4 \\
\bar{n}_5 &= C_{41} \cdot \bar{n}_{41} + C_{42} \cdot \bar{n}_{42} & \bar{n}_{42} &= \frac{s_{42}}{s_{41} + s_{42}} \bar{n}_4 \\
\bar{n}_6 &= C_5 \cdot \bar{n}_5 & \bar{n}_{61} &= \frac{s_{61}}{s_{61} + s_{62}} \bar{n}_6 \\
\bar{n}_7 &= C_{61} \cdot \bar{n}_{61} + C_{62} \cdot \bar{n}_{62} & \bar{n}_{62} &= \frac{s_{62}}{s_{61} + s_{62}} \bar{n}_6 \\
\bar{n}_8 &= C_7 \cdot \bar{n}_7 \\
\bar{n}_8 &= R \cdot n_8 + \bar{n}_{in}.
\end{aligned} \tag{33}$$

In the above equations we assumed that the split between the fluxes flowing in the core of the chamber and the annular region is proportional to the Santeler's probabilities in the respective regions. Solving the set of equations above for the flux at the thruster location n_3 we obtain the Flux model equation for the EP3 facility

$$\begin{aligned}
C_7 \cdot C_6 \cdot C_5 \cdot C_4 \cdot C_3 \cdot \bar{n}_3 &= \\
&= R \cdot C_7 \cdot C_6 \cdot C_5 \cdot C_4 \cdot C_3 \cdot C_2 \cdot C_1 \cdot L \cdot C_1^{-1} \cdot C_2^{-1} \bar{n}_3 + \bar{n}_{in}.
\end{aligned} \tag{34}$$

The Flux model predicts an overall pumping speed of 1,426,920 L/s for the EP3 facility. This value is approximately twice of the Node model estimate. The individual ring contributions to the overall pumping speed are shown in Table I. Unlike the Node model, where the individual contributions add up to the total pumping speed, the sum of the individual contributions in the Flux model adds up to 1,047,215 L/s, a number smaller than the total pumping speed predicted by the Flux model with all pumping surfaces active. This discrepancy is produced by redistribution of fluxes inside the chamber when not all rings (or pumps) are operating. Thus, while the Flux model is composed of linear equations, the resulting solution may produce a non-linear result. The Flux model predicts a total of 300,539 L/s as a contribution from the back side of the four rings (combined), which is 21% of the total

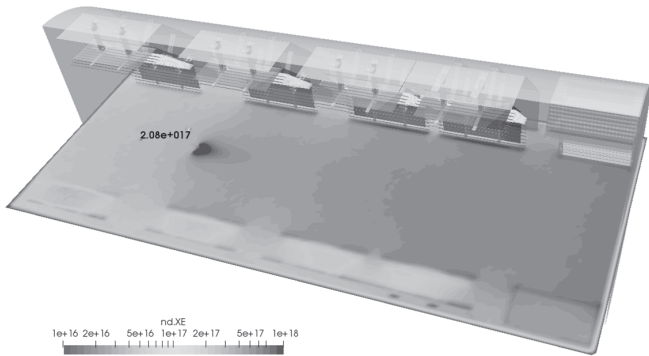


FIG. 12: Number density with a 20 kW thruster and pumps (left) and shroud (right)

pumping speed. Finally, the Flux model predicts 91,817 L/s as the pumping speed inside the fiberglass antechamber.

While the two models show significant disagreement, the complexity of the EP3 pumping configuration leads us to believe that the Node model, which does not account for all possible gas fluxes, may produce a conservative answer, while the Flux model result is more accurate. Thus, the actual pumping speed may be somewhere between the two values.

In order to gain more confidence in the analytical results we compared them to a detailed numerical simulation of the EP3 facility. The rarefied gas transport simulation program CTSP²⁰ was used for this study. The gas population within the chamber was represented with simulated particles that were injected at the thruster location. As CTSP does not contain a plasma simulation module, the thruster plume was approximated with a two-component drifting Maxwellian source. The two components corresponded to the primary high velocity populations and a smaller, more diffuse population of the slow-moving charge exchange ions. Particle positions were integrated through small time steps according to $\vec{x}^{k+1} = \vec{x}^k + \vec{v}^k \Delta t$. During each push, the code also checked for surface impacts. The chamber geometry was represented by a triangular surface mesh containing over 600,000 elements. This mesh was exported directly from a CAD drawing allowing us to retain small features that would likely be lost during the traditional meshing process. The surface elements were collected into several logical groups used to assign the particle impact behavior. The temperature of all surfaces was assumed to be 90K, with the exception of the chamber wall and the pumping cryo panels. The wall temperature was set to 290K, while the cryo panels were at 20K. Therefore, particles impacting any surface besides the cryo panels reflected back to the chamber. The post-impact velocity was obtained by sampling speed from the Maxwellian distribution at the surface temperature and direction from the cosine law about the surface normal. An 85% sticking coefficient was assumed on the cryo panels. The remaining 15% of molecules were re-emitted using the same model as used on all other surfaces.

Unlike Monte-Carlo ray-tracing codes, CTSP concurrently simulates the entire gas population in a manner similar to ap-

proaches found in PIC or DSMC. This allows the code to compute macroscopic gas parameters such as number density, partial pressure, or bulk velocity. Figure 12 shows the typical number density variation in the EP3 facility assuming a 20kW thruster. The grayscale shading on the cryogenic shroud sections indicates the relative amount of condensed mass indicating that the density (and hence pressure) is not uniform. While the density is the highest near the thruster, there is a secondary peak at the back wall due to the combined forward and return molecular flux. This particular simulation result was obtained assuming free-molecular flow, so collisions between the two populations were not considered. We can also observe a trapping effect of the LN2 louvers placed in front of the cryo panels. Furthermore, we can use this result to estimate the chamber pumping speed. From mass conservation, we have

$$\frac{\partial n}{\partial t} + \nabla \cdot (nu) = 0. \quad (35)$$

At steady state with constant density (which may not be a particularly good assumption), we have

$$(nuA)_1 = (nuA)_2, \quad (36)$$

where 1 and 2 are the total molecular flow rates in to and out of the chamber. The inflow is obtained from the thruster source mass flow rate, $(nuA)_1 = \dot{m}/m$. The product $uA = Q$, or the volumetric flow rate, which is also the pumping speed. Therefore, we can define

$$Q = \frac{\dot{m}}{m} \frac{1}{n}, \quad (37)$$

which can then be evaluated at various points using the local value of number density n . For instance, at the highlighted point, where $n = 2.08 \times 10^{17} m^{-3}$, we obtain $Q = 2.0$ ML/s. The thruster mass flow rate \dot{m} was calculated assuming 300 V discharge current and 100% ionization with no double ions.

V. CONCLUSIONS

In this paper we derived two analytical models for computing the pumping speed of a vacuum chamber. We specifically focused on the vacuum chamber configurations that are relevant for testing electric propulsion devices. The Node model was derived using a well-known calculation of the effective pumping speed adjusted by the conductance between the pump and the measurement location. We showed how this simple approach can be used for complex geometries. We found that in the two tested cases this approach produced reasonable agreement with the experimentally measured pumping speed. This model was then used to produce a conservative pumping speed estimate for the new vacuum chamber that is currently being designed.

We derived the Flux model by balancing particle fluxes with two temperatures. The two temperature approach was necessitated by the chamber surface temperatures – one at the ambient condition, such as the chamber walls, and second at a cold

temperature indicative of the cryo-pumps. The Flux model consists of two component matrices – the boundary condition matrices (left and right) and the cylindrical section matrix. These matrices can be combined in an appropriate fashion to simulate most of the relevant chamber geometries. The Flux model produced a good agreement with the experimen-

tally measured pumping speed for the two chambers investigated in this paper. The Flux model prediction of the pumping speed for the new chamber was twice as high as the pumping speed predicted by the Node model and within 30% of the PIC model results.

-
- [1] R. Spektor, W. G. Tighe, P. H. Stoltz, and K. R. C. Beckwith. Facility effects on Hall thruster performance through cathode coupling. Presented at The 34rd International Electric Propulsion Conference, Kobe, Japan, 6–10 July 2015, IEPC-2015-309.
- [2] K. Diamant, R. Spektor, E. J. Beiting, J. Young, and T. J. Curtiss. The effects of background pressure on Hall thruster operation. Presented at The 48th AIAA/ASME/SAE/ASEE Joint Propulsion Conference (JPC), Atlanta, GA, July 29 – August 1 2012, AIAA-2012-3735.
- [3] K. Diamant, R. Liang, and R. Corey. The effect of background pressure on SPT-100 Hall thruster performance. Presented at The 50th AIAA/ASME/SAE/ASEE Joint Propulsion Conference, Cleveland, Oh, July 28-30, 2014, AIAA-2014-3710.
- [4] K.D. Diamant, T. J. Curtiss, R. Spektor, E. J. Beiting, V. Hruby, B. Pote, J. Kolencik, and S. Paintal. Performance and plume characterization of the BHT-1500 Hall thruster. Presented at The 34rd International Electric Propulsion Conference, Kobe, Japan, 6–10 July 2015, IEPC-2015-069.
- [5] W. G. Tighe, R. Spektor, and R. Liang. The emi dependence on facility chamber pressures using the SPT-140 DM4 hall current thruster. ISPC-2016-3125288, Presented at The 5th Space Propulsion Conference, Rome, Italy 2016.
- [6] R. Hofer and J. Anderson. Finite pressure effects in magnetically shielded Hall thrusters. Presented at The 50th AIAA/ASME/SAE/ASEE Joint Propulsion Conference, Cleveland, Oh, July 28-30, 2014, AIAA-2014-3709.
- [7] H. Kamhawi, W. Huang, and T. Haag. Investigation of the effects of facility background pressure on the performance and operation of the high voltage hall accelerator. Presented at The 50th AIAA/ASME/SAE/ASEE Joint Propulsion Conference, Cleveland, Oh, July 28-30, 2014, AIAA-2014-3707.
- [8] A. Roth. *Vacuum Technology*. North-Holland, 3rd edition, 1990.
- [9] D. J. Santeler. New concepts in molecular gas flow. *J. Vac. Sci. Technol A.*, 4(3):338–343, May/June 1986.
- [10] C. Cai, I. D. Boyd, and Q. Sun. Free molecular background flow in a vacuum chamber equipped with two-sided pumps. *J. Vac. Sci. Technol A.*, 24(1):9–19, Jan/Feb 2005.
- [11] J. Frieman, T. M. Liu, and M. Walker. Background flow model of hall thruster neutral ingestion. *J. Prop. Power*, 33(5):1087–1101, September-October 2007.
- [12] C. Barnes. Cryopumping. Proceedings of the 1968 summer study on superconducting devices and accelerators, Brookhaven National Laboratory, NY, June 10– July 19, 1968, p. 230.
- [13] [https://en.wikipedia.org/wiki/Hadamard_product_\(matrices\)](https://en.wikipedia.org/wiki/Hadamard_product_(matrices)).
- [14] S. Goutelle, M. Maurin F. Rougier, X. Barbaut, L. Bourguignon, M. Ducher, and P. Maire. The hill equation: a review of its capabilities in pharmacological modelling. *Fund. and Clin. Pharm.*, 22(6):633–648, November 2008.
- [15] C. E. Garner, J. R. Polk, J. R. Brophy, and K. Goodfellow. Methods for cryopumping xenon. Presented at the 32nd AIAA/ASME/SAE/ASEE Joint Propulsion Conference (JPC), Lake Buena Vista, Fl, July 1–3, 1996, AIAA-1996-3206.
- [16] J.E. Pollard and E.J. Beiting. Ion energy, ion velocity, and thrust vector measurements for the SPT-140 Hall thruster. Presented at the 3rd International Conference of Spacecraft Propulsion, Cannes, France, October 10–13, 2000.
- [17] Cryopumps & refrigerator systems. <http://www.phpk.com/cryopumps.html>.
- [18] R. Spektor and E. J. Beiting. Non-invasive plasma diagnostic inside a Hall thruster discharge. Presented at the 30th International Electric Propulsion Conference (IEPC), Florence, Italy Sep. 17–20, 2007. IEPC-2007-69.
- [19] R. Spektor, K.D. Diamant, E.J. Beiting, Y. Raitses, and N.J. Fisch. LIF measurements of the Cylindrical Hall Thruster plume. Presented at the 31st International Electric Propulsion Conference (IEPC), Ann Arbor, MI, USA Sep. 20–24, 2009. IEPC-2009-137.
- [20] L. Brieda. Molecular contamination modeling with CTSP. 1786(01). Proceedings of 30th International Symposium on Rarefied Gas Dynamics.